Energy & Environmental Science

PAPER

View Article Online
View Journal | View Issue

Cite this: *Energy Environ. Sci.*, 2015, **8**, 3718

Elucidating the structure of the magnesium aluminum chloride complex electrolyte for magnesium-ion batteries†

Pieremanuele Canepa,‡*[ab] Saivenkataraman Jayaraman,‡§[a] Lei Cheng,[c] Nav Nidhi Rajput,[d] William D. Richards,[a] Gopalakrishnan Sai Gautam,[ab] Larry A. Curtiss,[c] Kristin A. Persson[d] and Gerbrand Ceder*[be]

Received 29th July 2015,
Accepted 27th October 2015

DOI: 10.1039/c5ee02340h

www.rsc.org/ees

Non-aqueous Mg-ion batteries offer a promising way to overcome safety, costs, and energy density limitations of state-of-the-art Li-ion battery technology. We present a rigorous analysis of the magnesium aluminum chloride complex (MACC) in tetrahydrofuran (THF), one of the few electrolytes that can reversibly plate and strip Mg. We use *ab initio* calculations and classical molecular dynamics simulations to interrogate the MACC electrolyte composition with the goal of addressing two urgent questions that have puzzled battery researchers: (i) the functional species of the electrolyte, and (ii) the complex equilibria regulating the MACC speciation after prolonged electrochemical cycling, a process termed as conditioning, and after prolonged inactivity, a process called aging. A general computational strategy to untangle the complex structure of electrolytes, ionic liquids and other liquid media is presented. The analysis of formation energies and grand-potential phase diagrams of Mg–Al–Cl–THF suggests that the MACC electrolyte bears a simple chemical structure with few simple constituents, namely the electro-active species $MgCl^+$ and $AlCl_4^-$ in equilibrium with $MgCl_2$ and $AlCl_3$. Knowledge of the stable species of the MACC electrolyte allows us to determine the most important equilibria occurring during electrochemical cycling. We observe that Al deposition is always preferred to Mg deposition, explaining why freshly synthesized MACC cannot operate and needs to undergo preparatory conditioning. Similarly, we suggest that aluminum displacement and depletion from the solution upon electrolyte resting (along with continuous $MgCl_2$ regeneration) represents one of the causes of electrolyte aging. Finally, we compute the NMR shifts from shielding tensors of selected molecules and ions providing fingerprints to guide future experimental investigations.

Broader context

Electrical energy storage is a key technology for a clean energy economy, but currently requires significant improvement in energy density beyond the capabilities of traditional Li-ion batteries. Mg-ion batteries offer an exciting alternative in terms of the amount of energy that can be delivered, safety, manufacturing and disposal costs, with limited environmental impact. The electrochemical functions of the Mg-ion battery ultimately depend on the choice of the electrolyte, which is limited by the peculiar chemistry of Mg. To date, very few electrolytes can reversibly plate and strip Mg. The magnesium aluminum chloride complex (MACC) electrolyte can reversibly plate and strip Mg with significantly higher voltage (3.1 V) as compared to other electrolytes, but there is a pressing need to address critical questions about the structural evolution of this electrolyte during electrochemical cycling.

[a] *Department of Materials Science and Engineering, Massachusetts Institute of Technology, Cambridge, MA 02139, USA. E-mail: pcanepa@mit.edu, pcanepa@lbl.gov*
[b] *Materials Science Division, Lawrence Berkeley National Laboratory, Berkeley, CA 94720, USA. E-mail: gceder@lbl.gov, gceder@berkeley.edu*
[c] *Materials Science Division, Argonne National Laboratory, Argonne, IL 60439, USA*
[d] *Environmental Energy Technologies Division, Lawrence Berkeley National Laboratory, Berkeley, CA 94720, USA*
[e] *Department of Materials Science and Engineering, University of California Berkeley, Berkeley, CA 94720, USA*

† Electronic supplementary information (ESI) available: Phase-diagram details, calculation of the MACC ionic conductivity, NMR and calculation convergence details, Geometries of the MACC species and radial distribution functions of the electrolyte species. See DOI: 10.1039/c5ee02340h

‡ These authors contributed equally to this work.

§ Current address: The Chemours Company, 1007 N Market Street, Wilmington, DE 19899, USA.

1 Introduction

The success of clean energy sources is predicated on improvements in energy storage technologies. State-of-the-art Li-ion batteries, although instrumental in considerable advances in portable electronics, cannot cope with the minimum storage[1–4] and safety[5] requirements dictated by grid and transport applications.

A viable strategy for post-Li-ion technology is to replace Li with safer and earth-abundant Mg. Magnesium has the advantage of doubling the total charge per ion, which results in larger theoretical volumetric capacity compared to typical Li-ion batteries.[1–4,6,7] Most importantly, in Mg-ion batteries the intercalation architecture of the graphitic-anode for Li-ions is replaced by a high-energy density metal anode ($\sim$700 Ah l^{-1} and $\sim$3830 Ah l^{-1}, respectively).[1,3,4,6–8]

Notwithstanding the tantalizing advantages of Mg-ion technology, its distinct electrochemistry imposes serious limitations on the kind of electrolyte that can reversibly plate and strip Mg, and at the same time sustain high-voltage cathode materials. For example, Mg-ion electrolytes that are analogous to their Li-ion counterparts (*e.g.* $PF_6^-Li^+$) and solvents (*e.g.* propylene carbonate/dimethyl carbonate) irreversibly decompose at the Mg anode, producing passivating layers that are impermeable to Mg-ions, and inhibit further electrochemical activity.[9,10]

To circumvent this issue, efforts by Gregory *et al.*[3,11] demonstrated quasi-reversible Mg-plating from Grignard's reagents. Greater coulombic efficiencies and anodic stabilities were achieved by Aurbach and collaborators after many years of meticulous tuning of the organic magnesium aluminum chloride salts (organo-magnesium-chloride complexes) dissolved in ethereal solutions, namely the dichloro complex (DCC) and the "all phenyl complex" (APC).[2,10,12–20] Similarly, Shao *et al.*[21] achieved Mg deposition by combining $Mg(BH_4)_2$ and $LiBH_4$ in diglyme. The air-sensitivity and low anodic stability of previous Mg-ion electrolytes led Kim *et al.*[22] to propose a non-nucleophilic salt comprising $AlCl_3$ and hexamethyldisilazide magnesium chloride (HMDSMgCl). Recently, Mohtadi, Arthur, and co-workers at Toyota developed a series of halogen-free electrolytes based on Mg borohydride, boron-clusters, and carboranes, which are not corrosive and have relatively high anodic-stability $\sim$3.8–4.0 V.[23–25] Subsequently, Doe *et al.*[17,18] developed an inexpensive electrolyte termed magnesium aluminum chloride complex (MACC) which is formed by mixing two common inorganic salts, namely $AlCl_3$ with $MgCl_2$ in ethereal solutions. MACC possesses a relatively large anodic stability ($\sim$3.1 V) and good reversible Mg deposition/stripping. The MACC electrolyte is the focus of the current paper.

The good performance of an electrolyte is dictated by few but important parameters such as high coulombic efficiency, high anodic and cathodic stabilities, and high diffusivity of the ion carriers, which depend ultimately on the structural composition of the electrolyte at rest and during electrochemical cycling. In the present study we interrogate the MACC electrolyte composition with the goal of elucidating: (i) the functional species of the electrolyte, and (ii) the complex equilibria regulating the MACC speciation after prolonged electrochemical cycling, a process termed as conditioning,[4] and after inactivity, termed as aging.[20] Aiming to describe important macroscopic effects observed in electrochemical experiments from the ground-up, and provide an atomistic picture of the processes regulating the speciation in the MACC electrolyte at different electrochemical conditions, we explore the complex chemical space of Mg–Cl–Al–THF (with THF as tetrahydrofuran) combining density functional theory (DFT) with classical molecular dynamics (CMD) simulations. The computational strategy is general and suitable to other electrolytes, ionic liquids, and a variety of liquid media.

On the basis of previous experimental XRD, Raman and NMR observations[16] on the APC electrolyte, similar to MACC but with organic moieties on the Al^{3+} ion, it is speculated that $Mg_mAl_nCl_{[(2m)+(3n)]}$ comprises the magnesium chloride monomer, $[\mu\text{-}MgCl\cdot 5THF]^+$, the dimer $[\mu\text{-}Mg_2Cl_3\cdot 6THF]^+$ and $AlCl_4^-$ as counterion. While monomer and dimer ions are yet to be observed during electrochemical cycling in both MACC and APC, they are thought to be the active Mg^{2+} carriers during electrochemical cycling. Barile *et al.*[20] also speculated that higher order magnesium-chloro structures such as trimer and multimeric units may exist, and they are included in this study.

With the aid of density functional theory calculations and molecular dynamics we are able to show that the MACC electrolyte bears a simple chemical structure with very few species present. By knowing the stable species of the electrolyte, we elucidate the equilibria taking place in the electrolyte, showing that the Mg^{2+} carriers, $MgCl^+$ are continuously exchanged with $MgCl_2$ (and $AlCl_4^-$ with $AlCl_3$), and changes of these equilibria alter the observed electrochemical performance of the electrolyte. Finally, our results suggest some explanation for the phenomena of electrolyte aging and conditioning.

These findings are instrumental for progressing the development of the next generation of Mg-ion batteries. Particularly, we demonstrate the working of the MACC electrolyte, and also provide clear directions for the improvement of the electrolyte performance.

2 Methodology

2.1 *Ab initio* molecular solvation and periodic bulk calculations

Due to the importance of strong interactions between solvent molecules and the species in the MACC electrolyte, we model, using density functional theory (DFT), each magnesium-aluminum-chloride complex with an explicit solvent of THF molecules in the first solvation shell and an implicit model in the outer shells to describe long-range solvent–solvent interactions. The methodology is shown in Fig. 1, where 3 THFs are included in the first solvation shell of $MgCl^+$, while the domain indicated by the cyan halo depicts outer shells, which are modeled as a dielectric medium by the polarizable continuum model (PCM).[26]

According to Fig. 1 G_{PCM}, the Gibbs free energy of the fully solvated Mg–Cl–Al–THF clusters are set by eqn (1).

$$G_{PCM} = E_{PCM} + ZPE_{expl} + q_{expl} - TS_{expl} \quad (1)$$

where G_{PCM} and E_{PCM} represent the Gibbs free energy and total energy of the fully solvated complex (explicit solvent and implicit solvent, see Fig. 1), while ZPE_{expl}, q_{expl}, and TS_{expl} are the zero point

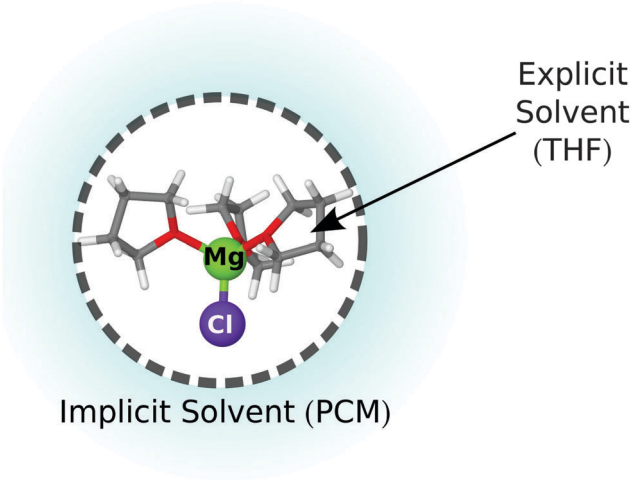

Fig. 1 Diagram showing the approximation used to capture the solvation structure of magnesium-aluminum-chloride complexes (see eqn (1)). Inner circle MACC cluster with a 1st shell of explicit solvent of THFs, outer circle (cyan halo) for longer range solvation shells.

energy correction, the thermal contribution, and the entropic term respectively, approximated by the MACC clusters comprising only the explicit solvent. To obtain the explicit part of E_{PCM} (see Fig. 1), we first relax the geometries of the magnesium-aluminum-chloro clusters (comprising an explicit 1st solvation shell of THFs) within the DFT approximation with B3LYP and a 6-31+G(d) basis-set implemented in Gaussian 09.[27] Previous battery studies have demonstrated that B3LYP can accurately reproduce experimental results.[28–31] More details on the methodology are provided in the ESI.† Finally, E_{PCM} of eqn (1) is obtained from a single point energy calculation on the relaxed structures using the PCM model.[26] Frequency analysis is performed to ensure that the relaxed structures are real minima as well as to compute the free energy corrections (*i.e.* ZPE_{expl}, q_{expl}, and TS_{expl}).

To evaluate some important reactions involving solid phases, we employ the B3LYP functional available in VASP.[32,33] The total energy is sampled on a well-converged $4 \times 4 \times 4$ *k*-point grid (and a $16 \times 16 \times 16$ *k*-point grid for Al and Mg metals) together with projector augmented-wave theory[34] and a 520 eV plane-wave cutoff. Forces on atoms are converged to less than 1×10^{-2} eV Å^{-1}. In order to compare the liquid species participating to chemical reactions containing solid phases (see Table 2) we simulated the relaxed structures obtained from molecular PCM calculations with periodic boundary conditions employing a box of size $20 \times 20 \times 20$ Å^3 and the VASP setup indicated above. Thus, the chemical potential of molecules and ions coordinated by THF (see Table 2) are referenced to the liquid THF *via* the experimental enthalpy of vaporization $\Delta H \sim 0.331$ eV.[35]

For relevant clusters, ^{35}Cl and ^{25}Mg NMR shielding tensors (only the isotropic shielding part is discussed) are provided as useful fingerprints to guide experiments. NMR parameters are obtained with Gauge-independent atomic orbital theory[36] on the relaxed structures at the 6-31+G(d) level of accuracy, but increasing the basis-set quality to 6-311+G(d,p). Basis-set convergence on the NMR isotropic shielding for these molecules are discussed in the ESI.†

2.2 Debye–Hückel correction

To account for the electrostatic interactions of ions in the electrolytic solution, we apply a potential energy correction to the reactions energies (see Table 2) based on Debye–Hückel theory.[37,38] Therefore the ΔE corrected by the Debye–Hückel model ΔE_{D-H} becomes:

$$\Delta E_{D-H} = \Delta E + \sum_{i=0}^{m} u_i \quad (2)$$

where ΔE obtained from DFT calculations at infinite dilution, m is the total number of ion i, and u_i the electrostatic potential energy given by eqn (3),

$$u_i = -\frac{z_i^2 e^2 \kappa}{8\pi\varepsilon_r\varepsilon_0}\frac{1}{1+\kappa a_0} \quad (3)$$

$$\kappa^2 = \sum_i \frac{z_i^2 e^2 c_i^0}{\varepsilon_r\varepsilon_0 k_B T} \quad (4)$$

where z_i is the charge number and c_i^0 the number concentration of ion i, ε_r the relative dielectric constant (7.58 for THF), ε_0 the vacuum permittivity, k_B the Boltzmann constant, T the temperature, e the electron charge, a_0 the minimum separation of ions, and κ^{-1} the Debye screening length. We set a_0 to be 7.1 Å that is the minimum separation of the van der Waals spheres of $MgCl^+$(3THF) and $AlCl_4^-$. Since the ΔE_{D-H} of eqn (3) depends on the ionic activity c_i^0, which in turn depends on the magnitude of the Debye–Hückel correction, the ΔE_{D-H} has to be evaluated numerically through an iterative self-consistent procedure. Self-consistency of u_i is achieved when the concentration (of the charged species, *i.e.* $MgCl^+$) equals the input concentration. In general, the Debye–Hückel theory is not appropriate for the description of concentrated solutions; for this reason we use the extended Debye–Hückel approximation (which holds for concentrations $<10^{-1}$ M), see eqn (3) and is compatible with the concentrations of the charged species in solution ($\sim$92 mM for $MgCl^+$ and $AlCl_4^-$).

2.3 Classical molecular dynamics simulations of bulk electrolytes

All classical molecular dynamics (CMD) simulations to study the dynamic structure of the MACC electrolyte are computed using LAMMPS[39] and treat the effect of the THF solvent explicitly. The THF–THF, and THF–ion interactions are modeled using the Generalized Amber Force Field[40,41] (GAFF), whereas Mg and Cl partial charges presented in Table 1 are computed with the RESP procedure by fitting the electrostatic potential surface of the optimized geometries using Antechamber.[40–42]

The GAFF force field parameters for THF were benchmarked against the experimental properties and found to reproduce the experimental values adequately. For example, the experimental density of THF ($\sim$0.889 g cm^{-3}) is well reproduced by CMD simulations ($\sim$0.882 g cm^{-3}),[28] similarly the experimental diffusion coefficient ($\sim 3.00 \times 10^{-5}$ cm^2 s^{-1}) is in good agreement with the calculated value ($\sim 2.11 \times 10^{-5}$ cm^2 s^{-1}).[28]

The MACC electrolyte structures initially optimized with Gaussian09 (see above) are inserted into a periodic box of size

Table 1 Computed RESP charges and van der Waals parameters (ε in kcal mol^{-1} and σ in Å) for Mg and Cl used in the classical CMD simulations of MACC electrolyte

Species	Mg	Cl
$MgCl_2$	0.9380	−0.4690
$MgCl^+$, monomer	1.4021	−0.4021[a]
$Mg_2Cl_3^+$, dimer	1.2621	−0.5081[a]
$Mg_3Cl_5^+$, trimer	1.1264	−0.4758[a]

Atom	ε	σ
Mg	0.88	1.64
Cl	0.71	4.02

[a] Compensating Cl^- counterions were assigned a charge of −1 to maintain charge neutrality.

48 × 48 × 48 Å^3 containing 800 THF molecules at the experimental THF density (0.889 g cm^{-3}). The infinite dilution limit is simulated for each complex, *i.e.* only one molecule was inserted in the CMD box. Then, each configuration is equilibrated for 1 ns in the isothermal–isobaric ensemble (*NPT*) which is sufficient to converge the density, with minimal variation (∼1%) from the THF experimental value. Subsequently, a 1 ns simulation is performed in the canonical ensemble (*NVT*) at 300 K, of which the first 200 ps is utilized for equilibration, within which convergence of each simulation is achieved, followed by a production time of 800 ps. A time step of 1 fs is used.

To identify how THF coordinates to the Mg_xCl_y (*i.e.* monomer, dimer and trimer) ionic species, it is not necessary to consider changes of the ion structures during coordination by THF. Therefore, in the CMD simulations the ions are held rigid (in the electrolyte solvent) at the fully relaxed geometries as obtained by Gaussian 09, thus removing the necessity of parameterizing bonded interactions of each ion.

3 Results

To isolate the electro-active species comprising the MACC electrolyte, we first study the structures and composition of various magnesium chloride complexes hypothesized to be present in the electrolyte. The Mg–Al–Cl–THF chemical space is further enlarged by additional structures that are guessed by chemical intuition or results of CMD simulations. Consequently, we study the salt solvation by altering the first solvation shell of the magnesium-chloro complexes considered. The ESI† reports the atomic positions of the thermodynamic stable structures.

3.1 Magnesium-chloride complexes

Previous experimental efforts have attempted to understand the complex structure of the magnesium-chloride complexes of the MACC electrolyte. The combined X-ray diffraction, Raman, and NMR spectroscopies by Aurbach and co-workers established that Mg^{2+} in THF exists always as a six coordinated ion in the form of monomer $MgCl^+$(5THF) or dimer $Mg_2Cl_3^+$(6THF).[14,16] In contrast to these results, a more recent theoretical investigation[43] elucidated the first solvation shell of the $MgCl^+$ and $Mg_2Cl_3^+$ magnesium organo-chloro species in the bulk electrolyte using *ab initio* molecular dynamics calculations, and suggested that the $MgCl^+$ monomer is always coordinated by three THFs, leading to a total Mg coordination of four. Similar findings were supported by the experimental NMR and XANES work of Nakayama *et al.*[44]

We benchmark our modelling strategy on previous experimental and theoretical results by simulating several magnesium-chloride complexes in different THF environments combining DFT and CMD calculations, as outlined above.

To measure the stability of magnesium-chloride clusters in THF we compute (with DFT) the formation free energy ΔF at fixed THF chemical potential μ_{THF}:

$$\Delta F = G(n_{Mg}, n_{Cl}, n_{THF}) - G(n_{Mg}, n_{Cl}) - n_{THF}\mu_{THF} \quad (5)$$

where $G(n_{Mg}, n_{Cl})$ and $G(n_{Mg}, n_{Cl}, n_{THF})$ of eqn (5) are the Gibbs free energy of each Mg_xCl_y cluster isolated and coordinated by n_{THF} molecules. Throughout the paper all references to "formation energy" refer to the formation free energy ΔF.

Fig. 2 depicts the free energies of formation ΔF for the magnesium-chloride complexes as a function of THF coordination (bottom *x*-axis) and total Mg coordination (top *x*-axis) obtained from B3LYP calculations.

Each minimum in Fig. 2 represents the most stable structure for a particular Mg–Cl complex, hence its most stable Mg coordination. Fig. 2 shows that the preferred magnesium coordination is 4-fold for both $MgCl^+$(3THF) and $MgCl_2$(2THF), 5-fold for the dimer $Mg_2Cl_3^+$(4THF), and 6-fold for the trimer $Mg_3Cl_5^+$(6THF). Interestingly, the total Mg coordination number increases with the size of the magnesium-chloride cluster. The stable structures show a coordination of 3THFs for the monomer $MgCl^+$ and 2 THFs for each Mg atom in dimer $Mg_2Cl_3^+$ (4THFs in total). These results are consistent with theoretical findings by Wan *et al.*[43] and XANES spectroscopy data.[44]

Classical molecular dynamic simulations are used to clarify the dynamics of the ion complexes in MACC in THF solvent.

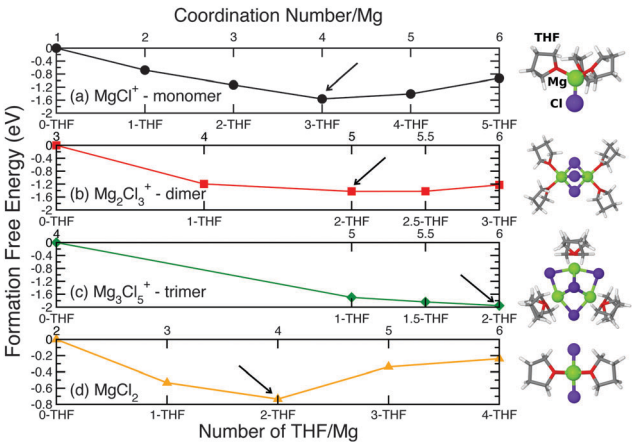

Fig. 2 Formation free energy (in eV) of magnesium-chloride complexes as a function of THF coordination for (a) $MgCl^+$ (monomer), (b) $Mg_2Cl_3^+$ (dimer), (c) $Mg_3Cl_5^+$ (trimer), and (d) $MgCl_2$. Arrows indicates the most stable THF coordination environment for each complex. Snapshots of the most stable magnesium-chloride complexes are also depicted.

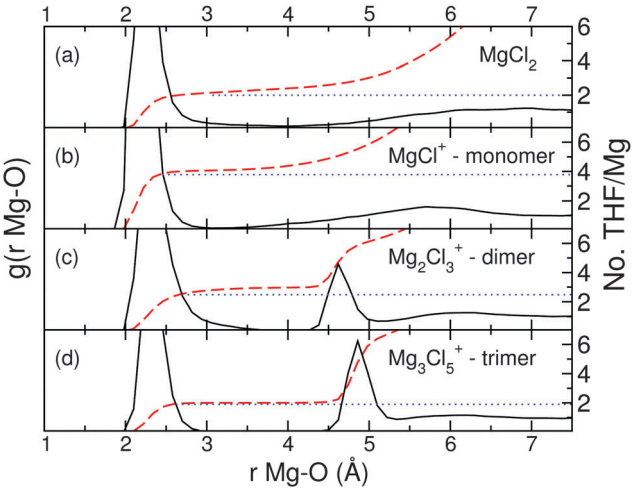

Fig. 3 Mg–O(THF) radial distribution function (black curves), and coordination numbers (red dashed lines) as function of the Mg–O separation (in Å) for the magnesium chloride-complexes. (a) $MgCl_2$, (b) $MgCl^+$ monomer, (c) $Mg_2Cl_3^+$ dimer, and (d) $Mg_3Cl_5^+$ trimer. The THF coordination numbers for the first coordination shell are indicated by the blue dotted lines.

Fig. 3 plots the radial distribution functions (RDF, black lines), and the corresponding coordination numbers for the 4 complexes (red and blue dashed and dotted lines, respectively) obtained from CMD calculations. More RDF plots of different atom pairs are available in the ESI.†

The peaks located between 2.0–2.5 Å in each RDF indicate the first coordination shell of Mg experienced by THF, and its integration (see blue dotted lines) the number of THF molecules coordinated by Mg atoms. For dimer and trimer of Fig. 3(c) and (d) the peaks from 4.5 to 5.0 Å are the oxygen atoms of the THFs coordinating the nearest neighbors Mg atoms. Fig. 3 obtained from classical molecular dynamic simulations, shows that the overall Mg coordination number for each Mg–Cl complex is consistent with the prediction from the DFT formation energies (see above). Our preliminary CMD simulations demonstrated that the coordination of $MgCl^+$ is wrongly predicted to be 6, if Mg^{2+} and Cl^- ionic charges are assigned to +2 and −1 for Mg and Cl ions, respectively.[43,44] This is because charge transfer processes occurring within each complex reduce the nominal charges on both Cl and Mg (as seen in Table 1), hence lowering the overall Mg coordination number to 4. Moreover, we find two kinds of Mg–THF coordinations observed for the charged ions–THF molecules are either strongly coordinated to the complex, or weakly coordinated, thereby setting up a free exchange of THF molecules with the bulk solution and the first solvation shell. For $Mg_2Cl_3^+$, two THF molecules are strongly coordinated to each Mg atom, while a third THF molecule is constantly exchanged between the bulk region and the Mg atoms in an alternating manner, leading to an effective coordination number of 2.5 THFs per Mg atom. For instance, this exchange occurs after 900 ps for $Mg_2Cl_3^+$. For the $MgCl^+$ monomer, the coordination number is predicted to be 3.7 THFs, and slightly larger than in previous *ab initio* MD simulations (3 THFs for $MgCl^+$).[43]

Overall, the coordination numbers computed from both DFT and CMD are consistent with previous XANES,[44] with sub-ambient pressure ionization nano-electrospray mass spectroscopy,[45] and accurate *ab initio* MD studies consolidating the idea that THF steric hindrances and Mg–Cl charge transfer lead to THF not being able to fulfill the typical sixfold coordination of Mg in solids.[43] To conclude, DFT coupled with computationally inexpensive CMD simulations provides a robust strategy to interrogate the structural characteristic of the species in the MACC electrolyte.

To study the effect of electrolyte composition on the stability of the MACC complexes, we analyze the stable phases of the Mg–Cl–Al–THF chemical space using the total energies of more than hundred Mg_xCl_y and Al_xCl_y molecules with variable THF coordination numbers.

Fig. 4 shows the grand-potential phase diagram[46] for the Mg–Cl–THF system at the bulk THF chemical potential, where black lines set the boundaries of the stable regions, and red-dots indicate the stable phases. To the best of our knowledge this is the first instance of grand-potential phase diagrams

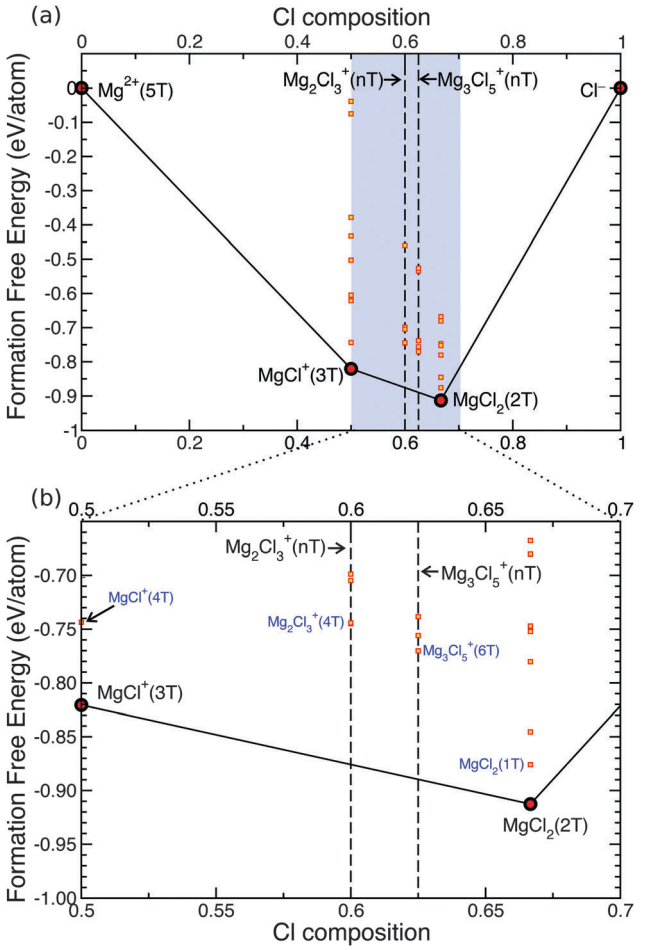

Fig. 4 (a) Mg–Cl–THF grand-potential phase diagram as function of Cl concentration at the bulk THF chemical potential. Red dots connected by black lines indicate the stable magnesium-chloride complexes, and unstable species by yellow squares. (b) Shows a region close to the stability lines. Coordinating THF molecules indicated by T. Dashed lines for the dimer and trimer concentrations.

together with DFT calculations being used to analyze the structure of a liquid electrolyte.

The THF chemical potential is calculated using the same procedure exposed in Section 3.1 from a cluster of 7 THF molecules extracted from an well equilibrated *ab initio* MD, see more details in ref. 47. The grand potential formation free energy of each complex is calculated with respect to Mg^{2+} in THF and Cl^{-} in THF as these are the relevant reference states for the complexes in THF. At Cl compositions of 0.0 (equivalent to 0% Cl and 100% Mg, or Mg^{2+}) and 1.0 (equivalent to 100% Cl and 0% Mg, or Cl^{-}), Mg^{2+} and Cl^{-} species are coordinated by 6 and 0 THFs, respectively. The formation free energies of Fig. 4 and successive grand-potential phase diagrams contain the vibrational entropy as indicated by eqn (1) and (5). Our calculations do not capture the configurational entropy that would tend to stabilize low coordination number. At first glance Fig. 4a and b show that solutions containing Mg and Cl in THF form stable magnesium-chloride complexes, and only $MgCl^{+}$(3T) (with T for THF) and $MgCl_2$(2T) are observed to be the stable phases (see red dots) through the entire Cl composition. We find that neither the dimer, nor the trimer are stable in bulk THF (see yellow squares marked as $Mg_2Cl_3^{+}$(4T) and $Mg_3Cl_5^{+}$(6T) for the dimer, trimer, respectively in Fig. 4b). Notably, the stable phases identified by the grand-potential phase diagram of Fig. 4 correspond to the lowest formation energies of the magnesium-chloride complexes as presented in Fig. 2. As already mentioned, the dimer $Mg_2Cl_3^{+}$ was isolated with X-ray on mono-crystals as one of the products of crystallization of the APC electrolyte,[16] while trimer and higher order structures were speculated to exist by Barile *et al.*[20] as a byproduct of polymerization of the principal MACC components $MgCl_2$, monomer and dimer.

By isolating the most stable Mg_xCl_y components from the grand-potential phase diagram of Fig. 4 we can estimate the reaction energies to form dimer and trimer complexes from the $MgCl^{+}$. Fig. 5 clearly shows that both dimer and trimer are not accessible in normal thermodynamic conditions (with almost 1 eV to create the trimer from the monomer). Hence our results argue against the existence of such magnesium-chloride agglomerates in the actual solution.[16,18,20,48]

To explore the morphology of the MACC electrolyte further and analyze possible changes that might occur to its structure, we investigate the stability of the electrolyte with varying THF chemical potential, and therefore look for possible conditions under which unstable structures from Fig. 4 can be stabilized (*e.g.* dimer and trimer).

Fig. 6 shows the grand-potential phase diagram[46] for the Mg–Cl–THF system at the chemical potential corresponding to

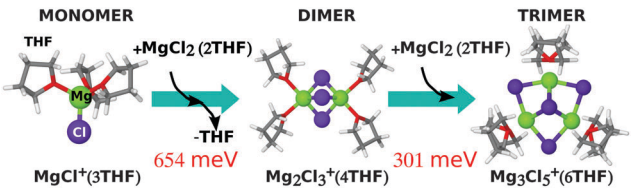

Fig. 5 Chemical reaction for monomer converting into dimer and trimer, with relative free energy (in meV).

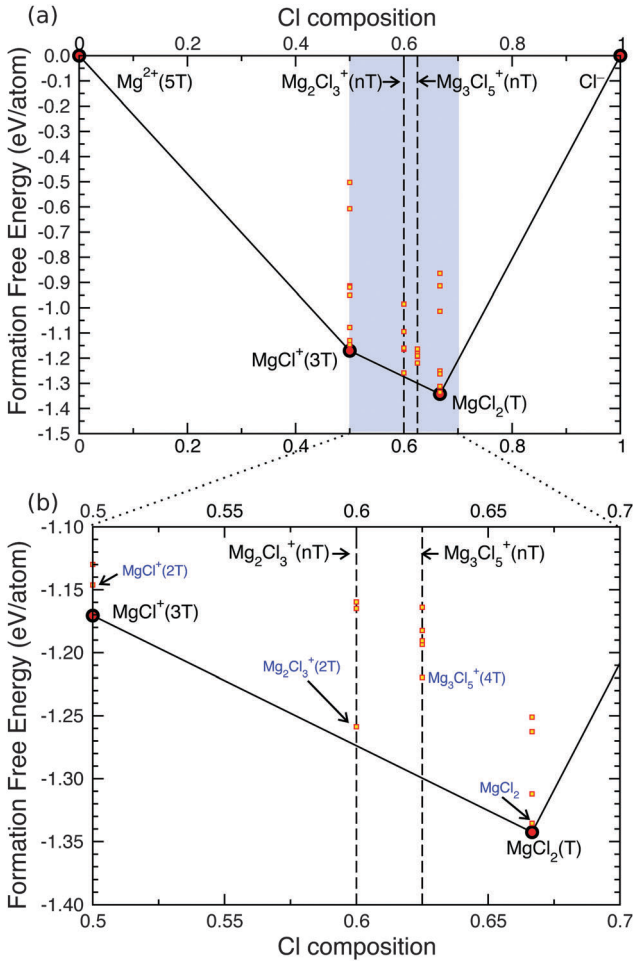

Fig. 6 (a) Mg–Cl–THF grand-potential phase diagram as function of Cl concentration at the THF chemical potential under drying conditions (with activity of THF = 10^{-6}). Red dots connected by black lines indicate the stable magnesium chloride complexes, and unstable species are indicated by yellow squares. (b) Shows a region close to the stability lines. Coordinating THF molecules indicated by T. Dashed lines as guide for dimer and trimer concentrations.

a THF activity of 10^{-6} (which means lowering the THF chemical potential by ~ -34.25 kJ mol^{-1}). Changing the THF chemical potential affects directly the relative stability of the THF coordination environment experienced by the MACC complexes, and low-coordination situations are preferred at low THF chemical potentials. For example, the THF coordination of $MgCl_2$ decreases from 2THF to 1THF, but the relative stability order between $MgCl_2$ and $MgCl^{+}$ is maintained. Lowering the chemical potential of THF in the bulk solution emulates the process of drying, where the solvent evaporates, and thereby only the strongly-bound THF molecules remain coordinated to the complexes.

Interestingly, from Fig. 6 we notice that the free energy of the dimer complex now approaches the ground state line (see black line), meaning that this structure might become accessible under conditions of evaporating/drying solvent. The dimer is only $\sim$0.02 eV above the stability line that is enough to be accessible by thermal fluctuations, and may explain why

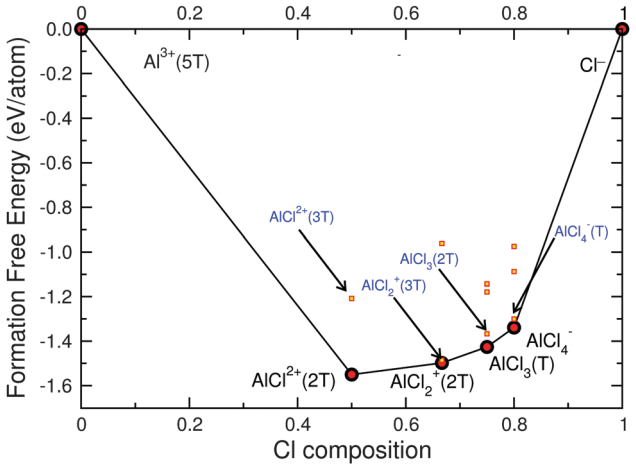

Fig. 7 Al–Cl–THF grand-potential phase diagram as function of Cl concentration at the THF chemical potential. Red dots connected by black lines indicate the stable magnesium-chloride complexes, and unstable species are indicated by yellow squares. Coordinating THF molecules are indicated by T.

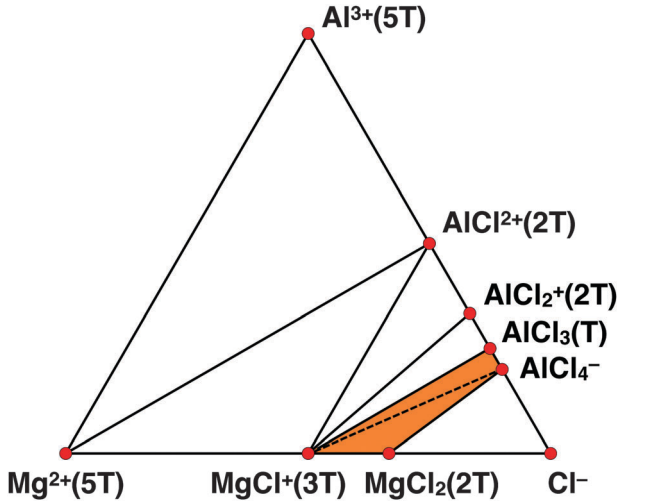

Fig. 8 Liquid phase Al–Cl–Mg–THF grand-potential phase diagram at the THF chemical potential. Red dots connected by black lines indicate the stable magnesium- and aluminum-chloride complexes. Coordinating THF molecules are indicated by T. Orange area and dashed line indicate the exchange reaction (c) (see Table 2 and text for more details). Tie-lines do not necessary respect charge neutrality (see text and ESI†).

the dimer was successfully crystallized.[16] In summary our results show that in pure Mg–Cl–Al–THF solutions neither the dimer nor the trimer exist at equilibrium, but a reduction of the THF chemical potential, as experienced in drying, may lead to the formation of dimers.

3.2 Aluminum complexes in THF and Al–Cl–Mg phase diagram

To complete the thermodynamic analysis of the possible species in the MACC electrolyte we perform a similar study of Al–Cl in THF. Fig. 7 shows the Al–Cl–THF grand-potential phase-diagram, where at Cl compositions of 0.0 and 1.0 are located the isolated species of Al^{3+} and Cl^- coordinated by 5 and by 0 THFs, respectively.

Fig. 7 suggests that the stable species in the electrolyte are: $AlCl^{2+}$(2THF), $AlCl_2^+$(2THF), $AlCl_3$(THF) and $AlCl_4^-$, with no Al_xCl_y polymeric species found to be stable in THF. Fig. 7 also captures the coordination of the aluminum chloride species by THF, with fourfold coordination for $AlCl_3$(THF); $AlCl_4^-$ being already fourfold coordinated does not have strongly bonded THF molecules.

Fig. 8 shows the ternary Al–Cl–Mg grand-potential phase-diagram at the THF chemical potential and black lines indicate tie-lines (more detail in the ESI†). Although the ternary Al–Cl–Mg grand-potential phase-diagram shows tie-lines such as Mg^{2+}–$AlCl_2^+$(2THF), $MgCl^+$(3THF)–$AlCl_2^+$(2THF), and $MgCl^+$(3THF)–$AlCl^{2+}$(2THF) these species cannot co-exist as they do not respect the charge neutrality of the MACC electrolyte. The orange part of the phase-diagram in Fig. 8 represents the zone where ionic species can co-exist and respect charge neutrality. Therefore, from the Al–Cl–THF grand-potential phase-diagram we deduce that the important equilibria will only occur among $MgCl^+$, $AlCl_4^-$ and $MgCl_2$ and $AlCl_3$ species and the dashed tie-line indicate their interaction. In the orange area, the only plausible equilibria that respect charge neutrality are either $MgCl^+$(3THF) with $AlCl_4^-$ or $MgCl_2$(2THF) with $AlCl_3$(THF). We use a dashed line for the interaction between $MgCl^+$(3THF) and $AlCl_4^-$ to indicate the small driving force of this reaction (see ΔE_{D-H} of reaction (c) in Table 2), which will be discussed in more detail later. The stable composition of the MACC electrolyte is the $MgCl^+$(3THF) and $AlCl_4^-$ tie-line.

Despite the small dielectric constant of THF ($\sim$7.58 at 298 K), from the phase diagram of Fig. 8 we do not find stable ionic couples (*e.g.* $MgCl^+$ $AlCl_4^-$) that would hinder the electrochemical function of the electrolyte. For example, the formation free energy of the monomer and the dimer ionic couples $[MgCl\cdot(3THF)]^+AlCl_4^-$ and $[Mg_2Cl_3\cdot(4THF)]^+AlCl_4^-$ require 0.064 eV and 0.088 eV, respectively.

3.3 MACC under equilibrium and conditioning

We use the knowledge of the stable species gained from grand-potential phase diagrams to explain the phenomenological effects observed in the MACC electrolyte under electrochemical cycling.

MACC electrolytes exhibit high coulombic efficiency, but only after extensive electrochemical cycling, a process termed conditioning.[4] Barile *et al.*[20] demonstrated that when a conditioned MACC electrolyte is left to rest for a prolonged period of time it shows lower coulombic efficiencies than when conditioned, and referred as "aging" of the electrolyte. The changes in the electrolyte species caused by aging and conditioning can be rationalized by evaluating possible reaction equilibria occurring in bulk and at the electrodes summarized in Table 2. The grand-potential phase diagrams in Fig. 4 and 6–8 attest to the presence of only four stable magnesium/aluminum chloride species, $MgCl_2$, $MgCl^+$, $AlCl_3$ and $AlCl_4^-$ limiting the total number of species in the reactions of Table 2. Here, we do not consider the ionic dissociation of $MgCl_2(AlCl_3)$ in $Mg^{2+}(Al^{3+})$ and Cl^- because of their

Table 2 Possible reaction equilibria of the Al–Cl–Mg–THF system, ΔE and corrected by Debye–Hückel ΔE_{D-H} (in eV). ΔE are computed from the total energy (E_{PCM} for liquid molecules) of each species

Reaction		ΔE	ΔE_{D-H}
$MgCl_2(s) + 2THF(l) \leftrightarrow MgCl_2(2THF)(l)$	(a)	0.251	—
$AlCl_3(s) + THF(l) \rightarrow AlCl_3(THF)(l)$	(b)	−1.138	—
$MgCl^+(3THF)(l) + AlCl_4^-(l) \leftrightarrow MgCl_2(2THF)(l) + AlCl_3(THF)(l)$	(c)	−0.106	0.085
Mg displacement of Al		ΔE	ΔE_{D-H}
$2AlCl_3(THF)(l) + 3Mg(s) + 4THF(l) \rightarrow 3MgCl_2(2THF)(l) + 2Al(s)$	(d)	−2.186	—
$AlCl_4^-(l) + MgCl^+(3THF)(l) + 1.5Mg(s) + 2THF(l) \rightarrow 2.5MgCl_2(2THF)(l) + Al(s)$	(e)	−1.199	−1.033

high-energy in our simulations. In addition, DFT calculations and *ab initio* MD dynamics confirm that Cl^- is poorly coordinated by THF.

The reaction energy (ΔE) at the dilute limit, and with the Debye–Hückel correction (ΔE_{D-H}) are included in Table 2. The Debye–Hückel correction captures the electrostatic interaction of charged species in solution at dilute activities, and stabilizes the ions in the electrolyte, thus affecting some reaction energies of Table 2. By fixing the MACC concentrations at the typical experimental value of 0.5 M,[18] the computed ΔE_{D-H} correction for reactions (c) and (e) is substantial and ∼0.1914 eV. As discussed in the methodology section, the ΔE_{D-H} is set by the initial ionic activity of $MgCl^+$, which in turn depends on the Debye–Hückel correction – the ΔE_{D-H} has to be computed numerically through an iterative self-consistent procedure. The initial concentration for $MgCl^+$ used to converge self-consistently ΔE_{D-H} (and $AlCl_4^-$) was set to ∼100 mM from which the converged ΔE_{D-H} is ∼0.1914 eV and gives a final $MgCl^+$ (and $AlCl_3$) concentration of ∼92 mM. The concentrations of the other species are discussed in the ESI.†

Reaction (a) of Table 2 dictates the equilibrium of $MgCl_2$ between its liquid and solid state, a reaction which is predicted as endothermic. The magnitude of the ΔE shows that $MgCl_2$ is sparingly "dissolved" in ethereal organic solvents such as THF or glymes and is supported by previous experimental evidences.[18,49] Reaction (b) that sets the "dissolution" of $AlCl_3$ in THF, is highly exothermic suggesting that $AlCl_3$ occurs in liquid THF.

In order to maintain charge neutrality, the activities of the charged species in solution, namely $MgCl^+(3THF)(l)$ and $AlCl_4^-(l)$, must remain equal, and this condition is regulated by reaction (c) of Table 2. Reaction (c) is slightly exothermic, favoring the formation of neutral molecules ($MgCl_2$ and $AlCl_3$) in the electrolyte. Nevertheless, when the Debye–Hückel correction is applied to reaction (c), the formation of ions is favored guaranteeing the operability of the MACC electrolyte. This stresses the importance to include the effect of the ion activities to compute properly reaction energies in liquids. Moreover, for the ionic strengths of $MgCl^+$ in the MACC electrolyte (92 mM), the extended Debye–Hückel model is sufficient.

The conductivity of the MACC electrolyte is related directly to the concentration of the ionic species $MgCl^+$, and $AlCl_4^-$. The slightly endothermic nature of reaction (c) ΔE_{D-H} shows that under thermodynamic equilibrium the charged species $MgCl^+$ and $AlCl_4^-$ are present in the electrolyte. At the solubility limit of $MgCl_2$ $\sim 7.8 \times 10^{-4}$ M in THF (set by reaction (a)) and for a 0.5 M of $AlCl_3$ in THF, the $MgCl^+$ activity is approximately 92 mM, which is high enough to guarantee good ionic conductivity (see discussion later). The Debye–Hückel correction on the ΔE of reaction (c) is concentration dependent (see eqn (4)) and is calculated as discussed above.

The processes of non-electrochemical Mg and Al deposition are regulated by reactions (d) and (e) in Table 2. Reaction (d) depicts the equilibrium between magnesium aluminum chloride neutral species and Mg and Al metals. The highly exothermic character of reaction (d) explains that Al deposition is preferred at the cost of Mg dissolution. A similar trend is observed for reaction (e) that establishes the equilibrium of charged and neutral magnesium aluminum chloride species and the respective metals. The reduction potential of Al (∼−1.67 V *vs.* NHE) is more positive than for Mg (∼−2.35 V *vs.* NHE) and ensures immediate Al deposition during initial electrochemical cycles. Spontaneous Al deposition sets a thermodynamic driving force for the process of aging, in absence of an applied potential at the electrode.

According to reactions (d) and (e) of Table 2 when a conditioned electrolyte is allowed to rest (*i.e.* not undergoing electrochemical cycling) the concentration of the electroactive species available in solution, $MgCl^+$ and $AlCl_4^-$, decrease by several orders of magnitude as Al ions in solutions are deposited on the electrode. Though the contribution of Debye–Hückel correction is substantial on the ΔE of reaction (e), it is not sufficient to stop Al deposition. We speculate that the spontaneous nature of reactions (d) and (e), along with concomitant parasitic polymerization reactions of the solvent at the Mg surface,[20] dictate the process of electrolyte aging.

On the basis of reactions (d) and (e) of Table 2, we suggest that during the first few electrochemical cycles of Mg deposition of a freshly prepared MACC electrolyte, Al ions in solution ($AlCl_4^-$) are easily displaced, thereby decreasing the initial coulombic efficiency of the electrolyte as observed by Barile *et al.*[20]—this process is called conditioning of the electrolyte (see discussion later). However, during conditioning the presence of a chemical or electrical potential promotes reaction (c) further towards the formation of $MgCl^+(AlCl_4^-)$ species, hence favoring Mg deposition over Al. The concepts of electrolyte aging and conditioning will be clarified further in the discussion section.

3.4 ^{25}Mg and ^{35}Cl NMR properties of selected Mg_xCl_y structures

To aid the interpretation of future NMR experiments on the MACC electrolyte we computed the NMR isotropic shielding

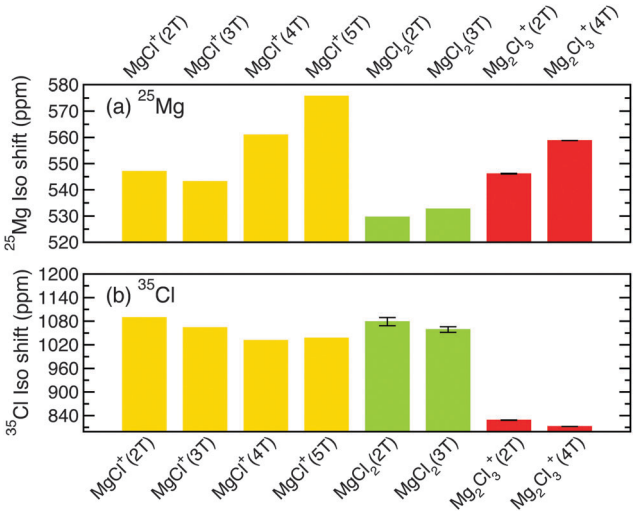

Fig. 9 (a) ^{25}Mg and (b) ^{35}Cl NMR isotropic shifts (in ppm) of relevant species magnesium-chloride complex ions in the MACC electrolytes. Colors indicate different magnesium-chloride complexes. Coordinating THF molecules indicated by T. Note that NMR data are not shifted to ^{25}Mg or ^{35}Cl standard reference compounds. Range of isotropic shifts for compounds with more than one Mg or Cl atoms is indicated by error bars.

fingerprints of ^{25}Mg and ^{35}Cl of selected MACC complexes. In general, changes in charge density localization on different MACC complexes directly alter the screening effects experienced by each NMR nucleus giving rise to different NMR responses.

While Mg posses an NMR active nucleus, due to its low abundance ^{25}Mg requires expensive high field NMR instruments. Therefore, in this analysis ^{25}Mg data will be complemented by data on the more abundant ^{35}Cl nucleus.

Fig. 9 shows the ^{25}Mg and ^{35}Cl NMR isotropic shifts in THF for some relevant Mg_xCl_y clusters isolated from the grand-potential phase diagrams of Fig. 4 and 6.

The ^{35}Mg and ^{35}Cl isotropic shielding (of Fig. 4) fall at very different absolute values. Note that NMR data of Fig. 9a and b are not shifted to ^{25}Mg and ^{35}Cl standard reference compounds.

Our results indicate that ^{25}Mg NMR should be able to distinguish very well between charged Mg_xCl_y complexes (*i.e.* $MgCl^+(n\mathrm{T})$ and $Mg_2Cl_3^+(n\mathrm{T})$) and neutral species ($MgCl_2(n\mathrm{T})$) in the MACC electrolyte. In addition we predict that ^{35}Cl NMR can discriminate between monomer and dimer species ($MgCl^+(n\mathrm{T})$ and $Mg_2Cl_3^+(n\mathrm{T})$), complementing ^{25}Mg NMR data. Though the combination of ^{25}Mg and ^{35}Cl NMRs can clearly differentiate between the stoichiometry of magnesium-chloride complexes, our calculations suggest that it will be more difficult to make conclusive claims on the effect played by the solvent (THF) with NMR. Furthermore, while the analysis of the Mg–Cl grand-potential phase-diagram suggests that agglomeration of $MgCl^+\cdots MgCl_2$ is significantly more likely to occur than the distinct dimer ($Mg_2Cl_3^+$, see discussion later), the spectroscopic differences between the two species may be subtle. For ^{25}Mg data an increase of the isotropic shift is observed for increasing THF coordination, see for example the trend for $MgCl^+(2\mathrm{T})$ to $MgCl^+(5\mathrm{T})$. Less pronounced is the ^{35}Cl NMR shift decrease as a response to an increase of the THF coordination number (see Fig. 9b).

4 Discussion

In this work, the stable species present in the MACC electrolyte are predicted using CMD and *ab initio* calculations.

Although this investigation provides an important understanding of the composition of the MACC electrolyte, it deals with bulk MACC solution and does not explicitly account for: (i) the effect of the anode and cathode surfaces, (ii) the existence of parasitic chemical reactions that might alter the electrolyte composition, and (iii) the presence of impurities.

From the formation energies and grand-potential phase diagrams of magnesium-chloride complexes we demonstrated that only two major Mg(Al) species are present at equilibrium conditions in MACC, namely the neutral $MgCl_2$ ($AlCl_3$) and electro-active $MgCl^+$ ($AlCl_4^-$). We demonstrate that larger Mg_xCl_y units such as dimer and trimer are not stable, though they might become accessible at room temperature by changing the solvent conditions (drying/crystallization). Polymerization of THF by $AlCl_3$ is also possible,[20,47] and has the effect of decreasing the solvating capabilities of THF towards the species in solution ($MgCl^+$ and $MgCl_2$). Therefore THF-polymerization represents an alternative mechanism to emulate drying conditions in solution and stabilize the dimer species. In drying conditions achieved with crystallization procedures, the dimer $Mg_2Cl_3^+$ has been successfully isolated,[16] but results in a electrochemically inert solution when redissolved in THF. Benzmayza *et al.*,[48] speculated that the lack of solvent in certain electrochemical conditions, for example when $MgCl^+$ and $MgCl_2$ approach the anode surface, is responsible for the formation of the dimer species. These experimental observations are consistent with our theoretical findings suggesting that the operation of the MACC electrolyte is ascribed to its simple chemical structure/composition, and regulated by uncomplicated equilibria.

Interestingly, previous theoretical investigations of the monomer and dimer coordination in THF[43] have demonstrated that the symmetry of the dimer is largely perturbed by the THF solvent, forming an open structure that resembles an isolated magnesium chloride molecule interacting with a dangling monomer, *i.e.* $MgCl_2\cdots MgCl^+$. Combining these observations, we speculate that the dimer $Mg_2Cl_3^+$ originates from the agglomeration of $MgCl_2$ available in solution and $MgCl^+$. Under conditions of drying/crystallization, similar agglomeration mechanisms can explain the formation of larger order magnesium-chloride structures (*e.g.* trimer and polymeric units), which have been speculated to exist.[20] To this end, we have computed useful ^{25}Mg and ^{35}Cl NMR fingerprints of the stable and unstable MACC species.

Our findings also shed light on the coordination of inorganic aluminum magnesium-chloride complexes. In line with preliminary experimental and theoretical work,[43–45] we demonstrate that magnesium-chloride salts in THF solutions cannot fulfill the typical 6-fold coordination of Mg^{2+} in solids, but always

prefer lower coordination numbers (*e.g.* 4-fold for the monomer $MgCl^+(3THF)$). According to the vast organic literature,[50–52] Grignard reagents' $MgXR_2$ (with X = Cl, Br) and halides salts ($MgCl_2$ and $MgBr_2$) in THF are typically found 4-fold coordinated, and confirm our findings. Compared to multi-dentate linear glymes (*e.g.* diglyme and tetraglyme) the ability for THF to coordinate ions is limited by the bulkier structure of the ring, and this has been also demonstrated experimentally and computationally by Seo *et al.*[53] Moreover, the coordination environment in the crystalline state does not necessarily reflect the coordination in the liquid phase.[54,55]

A closer analysis of our data shows that the stable Mg coordination number increases as a function of the Mg–Cl complex size from monomer to trimer. In a recent study, some of us attested that lower Mg^{2+} coordination numbers decreases the desolvation energy required to shed the solvent during plating and stripping.[47] We speculate that the larger Mg^{2+} desolvation energy for bigger Mg–Cl complexes (*e.g.* dimer and trimer) can inhibit the delivery of fresh Mg^{2+} at the Mg-anode during plating.

By identifying the principal species of the MACC electrolyte at equilibrium, $MgCl^+(3THF)$, $MgCl_2(2THF)$, $AlCl_4^-$, and $AlCl_3(THF)$, we can explain the phenomenological effects observed in the MACC electrolyte under electrochemical cycling. A thermodynamic analysis of the bulk electrolyte properties suggests that the equilibrium between $MgCl^+$ and $MgCl_2$ (and $AlCl_4^-$ and $AlCl_3$) in THF tends towards a solution dominated by charged $MgCl^+$ (and $AlCl_4^-$) species, (see reaction (c) Table 2 corrected by the Debye–Hückel model), which provides the appropriate conditions for ion conductivity. The ΔEs calculated for each equilibria dictate the activity ratio between $MgCl^+$ and $MgCl_2$ that impacts the number of charge carriers ($MgCl^+$) available in solution, and ultimately impacts the ionic conductivity of the MACC electrolyte. In MACC $AlCl_4^-$ functions as a shuttle replenishing Cl^- ions (at the anode surface) during Mg stripping (at the anode);[47] reaction (c) of Table 2 suggest that the ratio between $AlCl_4^-$ and $AlCl_3$ is large, hence allowing the complex dynamics of Mg stripping and dissolutions.

The availability of $MgCl^+$ in solution is not only controlled by reaction (c) but also depends on the low solubility of $MgCl_2$ in THF (see reaction (a)). Liao *et al.*[49] demonstrated that the solubility of $MgCl_2$ can increase dramatically provided the presence of Cl^- acceptors in solution. While $AlCl_3$ seems appropriate (as demonstrated by reaction (c)), other Cl^- ions acceptors can be introduced as "additives" (*e.g.* $Mg(HMDS)_2$) promoting large quantities of $MgCl^+$ in solution.

However, by using the Debye–Hückel corrected ΔE of reaction (c) we find that a significant concentration of charge carriers is still available in solution. For example using a typical concentration of 0.5 M for $AlCl_3$, and assuming that the maximum activity of soluble $MgCl_2$ in THF is 7.8×10^{-4} M (set by reaction (a)), we expect a concentration of $MgCl^+(3THF)$ in solution to be $\sim$92 mM. Notably, for this concentration we could derive, using the Kohlrausch's law for weak electrolytes, an ionic conductivity of 1.96 mS cm^{-1}, which is in excellent agreement with the experimental value measured by Doe *et al.* ($\sim$2 mS cm^{-1}) for a fully conditioned electrolyte.[18] See ESI† for the full derivation of the ionic conductivity.

The Al–Cl–Mg–THF phase diagram does not indicate the formation of stable $AlCl_4^- \cdots Mg_xCl_y^+$ ionic couples, though some of these clusters might be accessible within small energy windows (0.064–0.088 eV) with further repercussions on electrolyte conductivity. In general, the small dielectric constant of THF ($\sim$7.58) and glymes favor the formation of ionic couples, an indication that the next generation of solvents for Mg-ion batteries requires solvent with better screening properties.

Although we do not explicitly consider the Mg-electrode, from the reaction energy discussed in Table 2 we provide important considerations on the process of aging of the electrolyte. Fig. 10 summarizes the processes of aging (a) and conditioning (b) of the MACC electrolyte. From the equilibrium between Mg–Cl–Al species in solutions and Mg/Al bulk metals, we demonstrate that $AlCl_4^-$ ions in solutions are easily displaced during the initial stages of Mg deposition. In fact, Al deposition at the anode is ensured by a small Al reduction potential (~ -1.67 V *vs.* NHE) compared to Mg (~ -2.35 V *vs.* NHE) setting a thermodynamic driving force for the process of aging. Further aluminum depletion from the solution upon electrolyte resting, which impacts the amount of $MgCl^+$ in solution, could be one of the causes of aging of the MACC electrolyte. Additionally, parasitic polymerization reactions of the solvent have also been speculated[20] to be the source of electrolyte aging.

Under open circuit conditions (battery at rest), the reaction at the anode/electrolyte interface is largely controlled by the activity of $MgCl^+$ species available since reaction (c) dominates the composition of the electrolyte (see Table 2). Reactions (d) and (e) favor the formation of Al deposition under open circuit, leading to $AlCl_4^-$ (and $MgCl^+$) depletion form the solution, resulting in the aging of the electrolyte. However, when an aged electrolyte is subjected to charging, the presence of an applied potential drives Mg deposition on the anode, resulting in not only setting a concentration gradient of $MgCl^+(AlCl_4^-)$ from the bulk towards the anode (cathode) but also a continuous regeneration of $MgCl^+$ in the solution. After aging, the electrolyte will require a few charge–discharge cycles before the composition in the solution is stabilized and the charged species ($MgCl^+$ and $AlCl_4^-$) are abundantly present leading to smooth Mg deposition/stripping. Therefore, the state of conditioning in the electrolyte represents a transition between the Al-deposition regime (aging) and the Mg deposition/stripping regime during regular battery operation. Barile *et al.*[20] have estimated that about 100 electrochemical cycles are needed to condition the MACC electrolyte. This explains why low coulombic efficiencies of fresh MACC solutions have been attributed to Al deposition during the initial electrochemical cycles. SEM-EDS measurements of a Pt electrode that underwent Mg deposition during electrolyte conditioning showed large quantities of permanently deposited Al,[20] corroborating our modeling results.

Barile *et al.*[20] suggested that the MACC electrolyte is conditioned when the Mg/Al molar ratio in solution is $\sim$2.6 : 1, from which they concluded that dimer species must be present in the electrolyte. However, our grand-potential phase diagrams

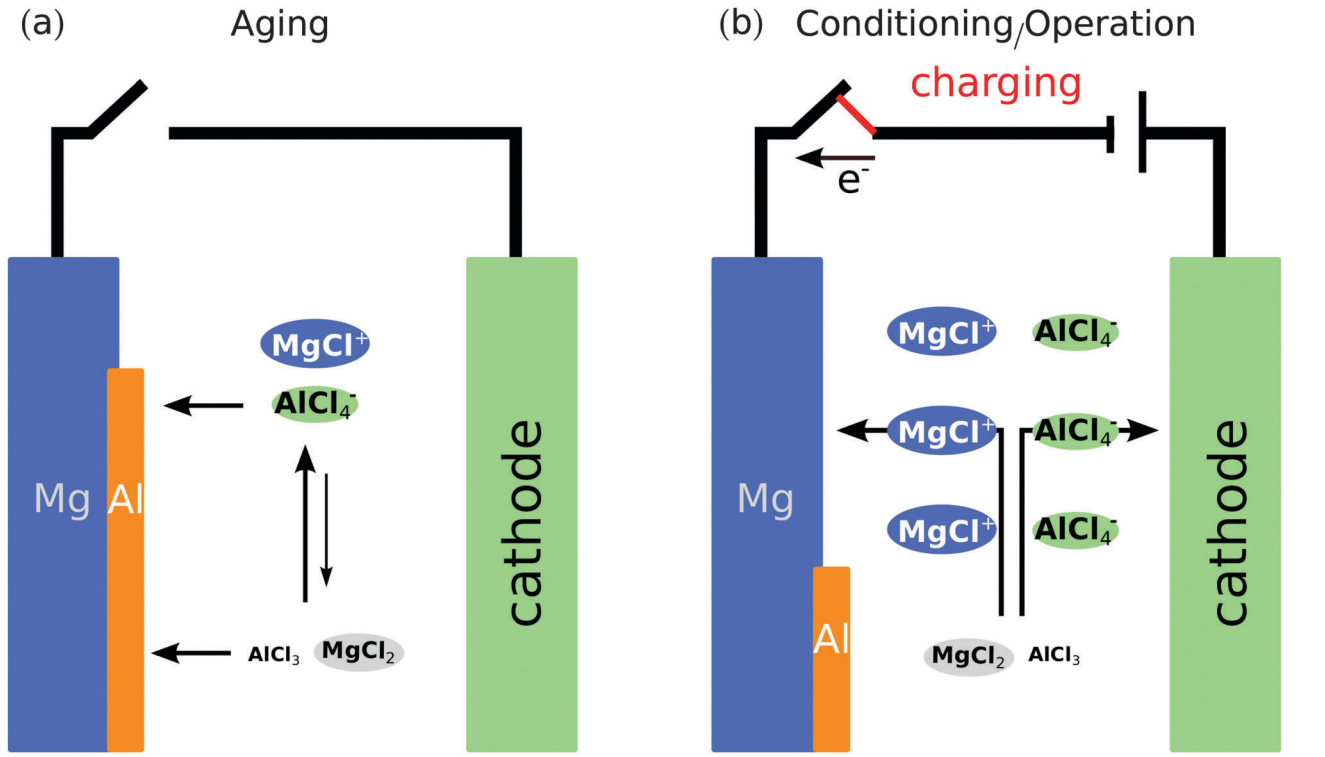

Fig. 10 Schematic of the processes of aging (a) and conditioning (b) of the MACC electrolyte in a battery setup. Panel (a) Al deposition at the Mg-anode electrode is depicted by orange stripes and supported by reactions (d) and (e) of Table 2. Panel (b) shows the activity gradients of $MgCl^+$ and $AlCl_4^-$ arising from the Mg plating process as well as continuous regeneration of these species in the bulk solution. During aging the species (*i.e.* $MgCl^+$, $MgCl_2$, $AlCl_4^-$, and $AlCl_3$) in solution are distributed homogeneously in the electrolyte.

(see Fig. 4 and 6) indicate that dimer species are unlikely to be present in the electrolyte at equilibrium, but only become accessible when drying or crystallizing the electrolyte. The Mg/Al ratio observed experimentally ($\sim$2.6 : 1) for conditioned electrolytes can alternatively stem from the presence of agglomerates $MgCl^+\cdots MgCl_2$ (the only stable species in solution) instead of distinct dimer ions – $MgCl^+\cdots MgCl_2$ clusters have been isolated previously using *ab initio* MD on a similar electrolyte.[43]

5 Conclusions

With the intention of elucidating the structural composition of the MACC electrolyte, we carried out *ab initio* calculations and classical molecular dynamics simulations on more than a hundred molecules and ions that could be structurally and functionally relevant for this electrolyte. We find that only $MgCl^+$, $MgCl_2$, $AlCl_4^-$ and $AlCl_3$ are stable constituents of the electrolyte. The thermodynamic analysis of the MACC composition excludes the presence of multimeric $Mg_xCl_y^+$ units such as dimer and trimer under equilibrium conditions. These species can be stabilized under conditions of solvent drying.

Equilibrium between the MACC species (*i.e.* $MgCl^+$ $MgCl_2$, $AlCl_4^-$ and $AlCl_3$) in liquid THF and Mg and Al metals suggests that Al is easily displaced from the solution during early Mg deposition cycles. This effect reduces the electrolyte coulobmic efficiency providing an explanation for the process of aging. In general, Al deposition on Mg–metal is always favored and leads to the more complex issue of electrolyte aging. We explain conditioning as the process which promotes the stabilization of charged species ($MgCl^+$ and $AlCl_4^-$) in solution due to a potential (chemical or applied), enabling Mg smooth deposition/stripping.

Computation of the NMR shifts of the relevant MACC species shows distinct ^{25}Mg and ^{35}Cl NMR signatures for monomer, dimer and $MgCl_2$, concluding that *in situ* NMR can clarify the composition of the MACC electrolyte as well as transformation of the MACC solution occurring during aging and conditioning of the electrolyte. Our analysis indicates that $MgCl_2$ is sparingly soluble in THF, but its solubility can be increased by introducing Cl^- acceptors.

Finally, the computational strategy adopted in this investigation is readily applicable in a high-throughput fashion to study other liquid media, specifically to progress the understanding of liquid electrolytes, and to screen for new electrolytes for the next generation of rechargeable batteries.

Acknowledgements

This work was fully supported as part of the Joint Center for Energy Storage Research (JCESR), an Energy Innovation Hub funded by the U.S. Department of Energy, Office of Science, and Basic Energy Sciences. This study was supported by

Subcontract 3F-31144. We also thank the National Energy Research Scientific Computing Center (NERSC), a DOE Office of Science User Facility supported by the Office of Science of the U.S. Department of Energy under Contract No. DE-AC02-05CH11231, for providing computing resources. PC and SJ are thankful to Dr Xiaohui Qu at the Lawrence Berkeley National Laboratory for numerous suggestions. All authors are also indebted to Dr Kevin R. Zavadil at Sandia National Lab, Dr Christopher Barile and Prof. Andrew Gewirth at University of Illinois Urbana-Champaign for stimulating discussions.

References

1 R. Van Noorden, *Nature*, 2014, **5**, 26–28.
2 H. D. Yoo, I. Shterenberg, Y. Gofer, G. Gershinsky, N. Pour and D. Aurbach, *Energy Environ. Sci.*, 2013, **6**, 2265–2279.
3 J. Muldoon, C. B. Bucur and T. D. Gregory, *Chem. Rev.*, 2014, **114**, 11683–11720.
4 I. Shterenberg, M. Salama, Y. Gofer, E. Levi and D. Aurbach, *MRS Bull.*, 2014, **39**, 453–460.
5 Y. S. Cohen, Y. Cohen and D. Aurbach, *J. Phys. Chem. B*, 2000, **104**, 12282–12291.
6 D. Aurbach, Z. Lu, A. Schechter, Y. Gofer, H. Gizbar, R. Turgeman, Y. Cohen, M. Moshkovich and E. Levi, *Nature*, 2002, **407**, 724–727.
7 J. Muldoon, C. B. Bucur, A. G. Oliver, T. Sugimoto, M. Matsui, H. S. Kim, G. D. Allred, J. Zajicek and Y. Kotani, *Energy Environ. Sci.*, 2012, **5**, 5941–5950.
8 M. Liu, Z. Rong, R. Malik, P. Canepa, A. Jain, G. Ceder and K. A. Persson, *Energy Environ. Sci.*, 2015, **8**, 964–974.
9 O. T. Brow and R. McIntyre, *Electrochim. Acta*, 1985, **30**, 627–633.
10 D. Aurbach and N. Pour, *Non-aqueous electrochemistry of magnesium (Mg)*, Woodhead Publishing Limited, 2011, vol. 1, ch. 13, pp. 484–515.
11 T. D. Gregory, R. J. Hoffman and R. C. Winterton, *J. Electrochem. Soc.*, 1990, **137**, 775–780.
12 D. Aurbach, R. Turgeman, O. Chusid and Y. Gofer, *Electrochem. Commun.*, 2001, **3**, 252–261.
13 D. Aurbach, H. Gizbar, A. Schechter, O. Chusid, H. E. Gottieb, Y. Gofer and I. Goldberg, *J. Electrochem. Soc.*, 2002, **149**, A115–A121.
14 H. Gizbar, Y. Vestfrid, O. Chusid, Y. Gofer, H. E. Gottieb, V. Marks and D. Aurbach, *Organometallics*, 2004, **23**, 3826–3831.
15 O. Mizrahi, N. Amir, E. Pollak, O. Chusid, V. Marks, H. Gottlieb, L. Larush, E. Zinigrad and D. Aurbach, *J. Electrochem. Soc.*, 2008, **155**, A103–A109.
16 N. Pour, Y. Gofer, D. T. Major and D. Aurbach, *J. Am. Chem. Soc.*, 2011, **133**, 6270–6278.
17 R. E. Doe, R. Han, Y. Gofer, D. Aurbach, N. Pour and E. Sterenberg, WO2013096827, 2013.
18 R. E. Doe, R. Han, J. Hwang, A. J. Gmitter, I. Shterenberg, H. D. Yoo, N. Pour and D. Aurbach, *Chem. Commun.*, 2014, **50**, 243–245.
19 C. J. Barile, R. Spatney, K. R. Zavadil and A. A. Gewirth, *J. Phys. Chem. C*, 2014, **118**, 10694–10699.
20 C. J. Barile, E. C. Barile, K. R. Zavadil, R. G. Nuzzo and A. A. Gewirth, *J. Phys. Chem. C*, 2014, **118**, 27623–27630.
21 Y. Shao, T. Liu, G. Li, M. Gu, Z. Nie, M. Engelhard, J. Xiao, D. Lv, C. Wang, J.-G. Zhang and J. Liu, *Sci. Rep.*, 2013, **3**, 3130.
22 H. S. Kim, T. S. Arthur, G. D. Allred, J. Zajicek, J. G. Newman, A. E. Rodnyansky, A. G. Oliver, W. C. Boggess and J. Muldoon, *Nat. Commun.*, 2011, **2**, 427.
23 O. Tutusaus, R. Mohtadi, T. S. Arthur, F. Mizuno, E. G. Nelson and Y. V. Sevryugina, *Angew. Chem., Int. Ed.*, 2015, **54**, 7900–7904.
24 T. J. Carter, R. Mohtadi, T. S. Arthur, F. Mizuno, R. Zhang, S. Shirai and J. W. Kampf, *Angew. Chem., Int. Ed.*, 2014, **53**, 3173–3177.
25 R. Mohtadi, M. Matsui, T. S. Arthur and S.-J. Hwang, *Angew. Chem., Int. Ed.*, 2012, **51**, 9780–9783.
26 J. Tomasi, B. Menucci and R. Cammi, *Chem. Rev.*, 2005, **105**, 2999–3094.
27 M. J. Frisch, G. W. Trucks, H. B. Schlegel, G. E. Scuseria, M. A. Robb, J. R. Cheeseman, G. Scalmani, V. Barone, B. Mennucci, G. A. Petersson, H. Nakatsuji, M. Caricato, X. Li, H. P. Hratchian, A. F. Izmaylov, J. Bloino, G. Zheng, J. L. Sonnenberg, M. Hada, M. Ehara, K. Toyota, R. Fukuda, J. Hasegawa, M. Ishida, T. Nakajima, Y. Honda, O. Kitao, H. Nakai, T. Vreven, J. A. Montgomery Jr, J. E. Peralta, F. Ogliaro, M. Bearpark, J. J. Heyd, E. Brothers, K. N. Kudin, V. N. Staroverov, R. Kobayashi, J. Normand, K. Raghavachari, A. Rendell, J. C. Burant, S. S. Iyengar, J. Tomasi, M. Cossi, N. Rega, J. M. Millam, M. Klene, J. E. Knox, J. B. Cross, V. Bakken, C. Adamo, J. Jaramillo, R. Gomperts, R. E. Stratmann, O. Yazyev, A. J. Austin, R. Cammi, C. Pomelli, J. W. Ochterski, R. L. Martin, K. Morokuma, V. G. Zakrzewski, G. A. Voth, P. Salvador, J. J. Dannenberg, S. Dapprich, A. D. Daniels, Ö. Farkas, J. B. Foresman, J. V. Ortiz, J. Cioslowski and D. J. Fox, *Gaussian 09 Revision D.01*, Gaussian Inc., Wallingford, CT, 2009.
28 N. N. Rajput, X. Qu, N. Sa, A. K. Burrell and K. A. Persson, *J. Am. Chem. Soc.*, 2015, **137**, 3411–3420.
29 S. P. Ong, O. Andreussi, N. Marzari and G. Ceder, *Chem. Mater.*, 2011, **23**, 2979–2986.
30 Y. Zhang, C. Shi, J. F. Brennecke and E. J. Maginn, *J. Phys. Chem. B*, 2014, **118**, 6250–6255.
31 M. Okoshi, Y. Yamada, A. Yamada and H. Nakai, *J. Electrochem. Soc.*, 2013, **11**, A2160–A2165.
32 G. Kresse and J. Hafner, *Phys. Rev. B: Condens. Matter Mater. Phys.*, 1993, **47**, 558.
33 G. Kresse and J. Furthmüller, *Phys. Rev. B: Condens. Matter Mater. Phys.*, 1996, **54**, 11169–11186.
34 G. Kresse and D. Joubert, *Phys. Rev. B: Condens. Matter Mater. Phys.*, 1999, **59**, 1758–1775.
35 D. Scott, *J. Chem. Thermodyn.*, 1970, **2**, 833–837.
36 K. Wolinski, J. F. Hinton and P. Pulay, *J. Am. Chem. Soc.*, 1990, **112**, 8251–8260.

37 P. Debye and E. Hückel, *Phys. Z.*, 1923, **24**, 185–206.
38 R. A. Robinson and R. H. Stokes, *Electrolyte Solutions: Second Revised Edition*, Butterworth & Co., London, 1968.
39 S. Plimpton, *J. Comput. Phys.*, 1995, **117**, 1–19.
40 J. Wang, R. M. Wolf, J. W. Caldwell, P. A. Kollman and D. A. Case, *J. Comput. Chem.*, 2004, **25**, 1157–1174.
41 J. Wang, W. Wang, P. A. Kollman and D. A. Case, *J. Mol. Graphics Modell.*, 2006, **25**, 247–260.
42 C. I. Bayly, P. Cieplak, W. D. Cornell and P. A. Kollman, *J. Phys. Chem.*, 1993, **97**, 10269–10280.
43 L. F. Wan and D. Prendergast, *J. Am. Chem. Soc.*, 2014, **136**, 14456–14464.
44 Y. Nakayama, Y. Kudo, H. Oki, K. Yamamoto, Y. Kitajima and K. Noda, *J. Electrochem. Soc.*, 2008, **155**, A754–A759.
45 T. Liu, J. T. Cox, D. Hu, X. Deng, J. Hu, M. Y. Hu, J. Xiao, Y. Shao and J. Liu, *Chem. Commun.*, 2015, **51**, 2312–2315.
46 S. P. Ong, L. Wang, B. Kang and G. Ceder, *Chem. Mater.*, 2008, **20**, 1798–1807.
47 P. Canepa, G. S. Gautam, R. Malik, S. Jayaraman, R. Ziqin, K. R. Zavadil, K. Persson and G. Ceder, *Chem. Mater.*, 2015, **27**, 3317–3325.
48 A. Benzmayza, M. Ramanathan, T. S. Arthur, M. Matsui, F. Mizuno, J. Guo, P.-A. Glans and J. Prakash, *J. Phys. Chem. C*, 2013, **117**, 26881–26888.
49 C. Liao, N. Sa, B. Key, A. K. Burrell, L. Cheng, L. A. Curtiss, J. T. Vaughey, J.-J. Woo, L. Hu, B. Pan and Z. Zhang, *J. Mater. Chem. A*, 2015, **3**, 6082–6087.
50 L. J. Guggenberger and R. E. Rundle, *J. Am. Chem. Soc.*, 1968, **90**, 5375–5378.
51 J. F. Garsta and M. P. Soriagab, *Coord. Chem. Rev.*, 2004, **248**, 623–652.
52 S. Pirinen, I. O. Koshevoy, P. Denifl and T. T. Pakkanen, *Organometallics*, 2013, **32**, 4208–4213.
53 D. M. Seo, P. D. Boyle, O. Borodin and W. A. Henderson, *RSC Adv.*, 2014, 8014–8019.
54 S. Ansell, S. Krishnan, J. K. R. Weber, J. J. Felten, P. C. Nordine, M. A. Beno, D. L. Price and M.-L. Saboungi, *Phys. Rev. Lett.*, 1997, **78**, 464.
55 P. Wernet, D. Nordlund, U. Bergmann, M. Cavalleri, M. Odelius, H. Ogasawara, L. A. Näslund, T. K. Hirsch, L. Ojamäe, P. Glatzel, L. G. M. Pettersson and A. Nilsson, *Science*, 2004, **304**, 995–999.

